Negative thermal expansion and photoluminescence in solid solution $(HfSc)_{0.83}W_{2.25}P_{0.83}O_{12-\delta}$*

Yuan Liang(梁源)[1,2,†], Yong-Guang Cheng(程永光)[2], Xiang-Hong Ge(葛向红)[2], Bao-He Yuan(袁保合)[2], Juan Guo(郭娟)[2], Qian Sun(孙强)[2], and Er-Jun Liang(梁二军)[2]

[1] *Department of Applied Physics, Donghua University, Shanghai* 201620, *China*

[2] *School of Physical Science & Engineering and Key Laboratory of Materials Physics of Ministry of Education of China, Zhengzhou University, Zhengzhou* 450052, *China*

(Received 18 May 2017; revised manuscript received 29 June 2017; published online 20 August 2017)

A solid solution of $(HfSc)_{0.83}W_{2.25}P_{0.83}O_{12-\delta}$ is synthesized by the high-temperature, solid-state reaction and fast-quenching method. It is shown that it possesses an orthorhombic structure with space group *Pmmm* (47) and exhibits negative thermal expansion (NTE) property with low anisotropy in thermal expansion. The coefficients of thermal expansion (CTEs) for *a*, *b*, and *c* axes are -1.41×10^{-6} K^{-1}, -2.23×10^{-6} K^{-1}, and -1.87×10^{-6} K^{-1}, respectively. This gives rise to volume and linear CTEs of -3.10×10^{-6} K^{-1} and -1.03×10^{-6} K^{-1}, respectively. Besides, it exhibits also intense photoluminescence from 360 nm to about 600 nm. The mechanism of NTE and the correlation of the PL with axial thermal expansion property are discussed.

Keywords: negative thermal expansion, solid solution, photoluminescence

PACS: 65.40.De, 81.05.Je, 61.50.–f, 78.55.–m **DOI:** 10.1088/1674-1056/26/10/106501

1. Introduction

Expansions on heating are general phenomena for gases, liquids, and solids but there are a few exceptions for liquids and solids such as water below 277 K and ZrW_2O_8 below 1050 K. Thermal expansion of gases has widely been used for energy conversion. Nevertheless, thermal expansions of solids in most cases have negative effects on devices such as deterioration in performance, and even failure when temperature is changed suddenly or greatly. Due to the fact that the vast majority of materials expand on heating and have different coefficients of thermal expansion (CTEs), thermal expansion and mismatch in CTES could cause serious problems, for example, thermal lensing effect or even cracking lenses used in high power lasers, center wavelength shifting in fiber Bragg gratings. In order to prevent these problems from being caused by thermal expansion, precision devices or instruments require a relatively constant temperature environment, or complex structure design to compensate for thermal expansion. Enough gap or space between two adjacent parts is usually obliged to be reserved in engineering. Materials with negative thermal expansion (NTE) can be used individually or as compositions to tailor CTEs of materials to zero or desired values. Due to the scientific curiosity and technical requirements, the discovery of NTE of ZrW_2O_8 in a large temperature range aroused much interest in NTE materials and related physics and chemistry behind the NTE phenomena.[1–10] Different mechanisms contributing to NTE were revealed for different categories of materials: magneto-volume effects in magnetic metals and alloys such as Invar and antiperovskite Mn_3AX (A = transition metals or semiconducting element; X = C or N);[11–13] charge-transfer-induced ionic radius contractions such as in $LaCu_3Fe_4O_{12}$[14] and $BiNiO_3$;[15] ferroelectric ordering-induced volume contractions such as in $PbTiO_3$;[3,16] and translational and librational vibration-induced contractions in framework structures such as ZrW_2O_8,[1,5,17] ZrV_2O_7,[18–20] $A_2M_3O_{12}$ (A = transition metal or rare earth, M = W or M),[7,8,21–24] ScF_3,[6,25] cyanides,[4,9] etc.

The advantages of $A_2M_3O_{12}$ family of materials are they exhibit NTEs in a relatively large temperature range and chemical flexibility in choosing the new substitutes for elements. The A^{3+} cation can be substituted by not only trivalent ions but also tetravalent and bivalent ones, while the M^{6+} can be not only W and/or Mo but also pentavalent cations. With such substitutions, thermal expansions and other physical properties can be tailored and even near zero thermal expansion materials can be designed.[26,27] Particularly, the success in the syntheses of ABM_3O_{12} (A = Zr, Hf; B = Mg, Mn; M = W, Mo),[28–34] and even more recently ABM_2XO_{12} (A = Zr, Hf; B = Sc; M = W, Mo; X = P, V)[35–38] have enriched the members of NTE materials as well as their functions such as high ionic conductivity[39] and intense photoluminescence (PL).[35–38] Most of the $A_2M_3O_{12}$ family of materials either exhibit monoclinic-to-orthorhombic phase tran-

*Project supported by the National Natural Science Foundation of China (Grant Nos. 11574276, 51302249, and 11405028) and the Fundamental Research Fund for the Central Universities, China.

†Corresponding author. E-mail: yliang@dhu.edu.cn

© 2017 Chinese Physical Society and IOP Publishing Ltd

sition (with smaller A^{3+} cation) well above room temperature (RT) or are highly hygroscopic (with larger A^{3+} cation) and their NTEs are observed only above the phase transition temperature or after the complete removal of crystal water. Even in the newly designed materials, $HfMgW_3O_{12}$[29] and $ZrMnMo_3O_{12}$[34] transform from monoclinic structure to orthorhombic structure above 400 K and 363 K, respectively, and $ZrMgW_3O_{12}$[31] is hygroscopic and $HfMgMo_3O_{12}$[32] shows low positive thermal expansion (PTE). To develop the NTE, the materials without phase transition above RT or hygroscopicity are desirable.

Inspired by the above developments in $A_2M_3O_{12}$ family of materials, we aim to design a novel NTE material with the formula of $HfScW_3PO_{15}$ in this paper. The x-ray diffraction (XRD) and elemental analyses suggest that the synthesized material crystallizes in a pure single phase with elemental compositions as designed but it possesses a structure similar to $HfScW_2PO_{12}$,[37] instead of $La_2Mo_4O_{15}$.[40] Combining the structural information and the result of elemental analysis, it is more reasonable to write its chemical formula as $(HfSc)_{0.83}W_{2.25}P_{0.83}O_{12-\delta}$ rather than $HfScW_3PO_{15}$. Further studies show that the solid solution of $(HfSc)_{0.83}W_{2.25}P_{0.83}O_{12-\delta}$ exhibits NTEs in all three axes, leading to a very low anisotropy in thermal expansion. Besides, it exhibits also intense PL in the visible region. These properties make it possible to be used in optical devices such as light emitting diodes. This work might pave the way for developing NTE materials with low thermal expansion anisotropies, which favor thermal shock resistances.[41]

2. Experiment

Analytical reagents HfO_2, Sc_2O_3, WO_3, and $NH_4H_2PO_4$ with a molar ratio of 1.0:0.5:3.15:1.0 were used as starting materials. They were mixed and ground in an agate mortar for 2 h and pressed into pellets by cold pressing. The pellets were sintered in a furnace at 1473 K for 2 h and then at 1573 K for 2.5 h with intermediate grinding. After sintering at 1573 K, the samples were taken out from the furnace and put into cold water quickly and then dried in an oven. Some of the pellets were ground into powder for x-ray diffraction (XRD) and x-ray photoelectron spectroscopy (XPS) analyses.

The surface morphology was observed with a Quanta 250 scanning electron micrograph (SEM, USA FEI). The temperature-dependent XRD data were collected on a Rigaku (SmartLab 3KW) diffractometer with Cu Kα radiation from 94 K to 573 K. The compositions of the sample were analyzed by XPS (Axis Ultra, Kratos, U.K.). A HORIBA Jobin-Yvon Lab RAM HR Evolution Raman spectrometer with 633-nm laser wavelength excitation was used for Raman spectral analysis. The absorption spectrum was measured with a SHIMADZU UV3600 UV-Vis-IR spectrophotometer. PL spectra from RT to 10 K were recorded by a Fluoromax-4 spectrofluorometer (HORIBA Jobin Yvon) with a Lake Shore 325 temperature controller. The linear CTEs for the low and high temperature ranges were measured with LINSEIS L75 and LINSEIS DIL L76 dilatometers, respectively.

3. Results and discussion

3.1. Structure analysis

Figure 1(a) shows the XRD pattern of powdered sample at room temperature (RT) (solid black curve). There are no diffraction peaks corresponding to secondary phases nor starting materials, indicating a single phase formation of the solid solution. Pawley analysis of the XRD pattern with the academic software of TOPAS 4.0 (indicated by the red symbols $\times$) shows that the best R-factors could be obtained using space group *Pmmm* (No. 47). The obtained R-factors are $R_p = 5.11\%$, $R_{wp} = 6.86\%$, $R_{exp} = 4.64\%$, and $\chi^2 = (R_{wp}/R_{exp})^2 = 2.19$, respectively. Each of the diffraction peaks can well be indexed as shown in Fig. 1(b) (only the results for 10° to 45° are presented for clarity). The lattice constants for the a, b, and c axes at RT are calculated to be 9.2939 Å, 9.4040 Å, and 12.9011 Å, respectively.

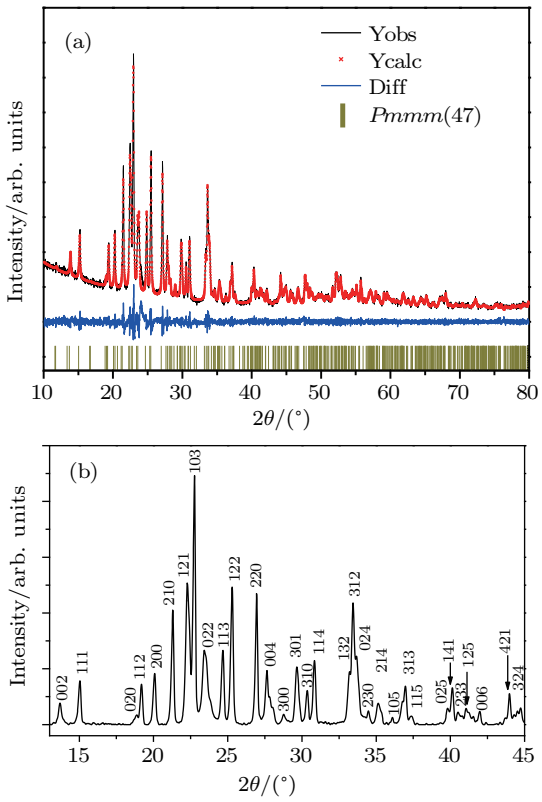


Fig. 1. (color online) Structure analysis of the sample: (a) XRD patterns of the powder sample at room temperature and the results of the Pawley analysis using space group *Pmmm* (No. 47) ($R_p = 5.11\%$, $R_{wp} = 6.86\%$, and $R_{exp} = 4.64\%$). The solid black line represents the observed profile. The "$\times$" signs represent the calculated profile. Vertical bars indicate the position of Bragg peaks for this phase; the blue curve in the middle is the difference between the observed and calculated patterns. (b) Indexes of the RT XRD pattern of the solid solution with the space group *Pmmm* (No. 47) from 10° to 45°.

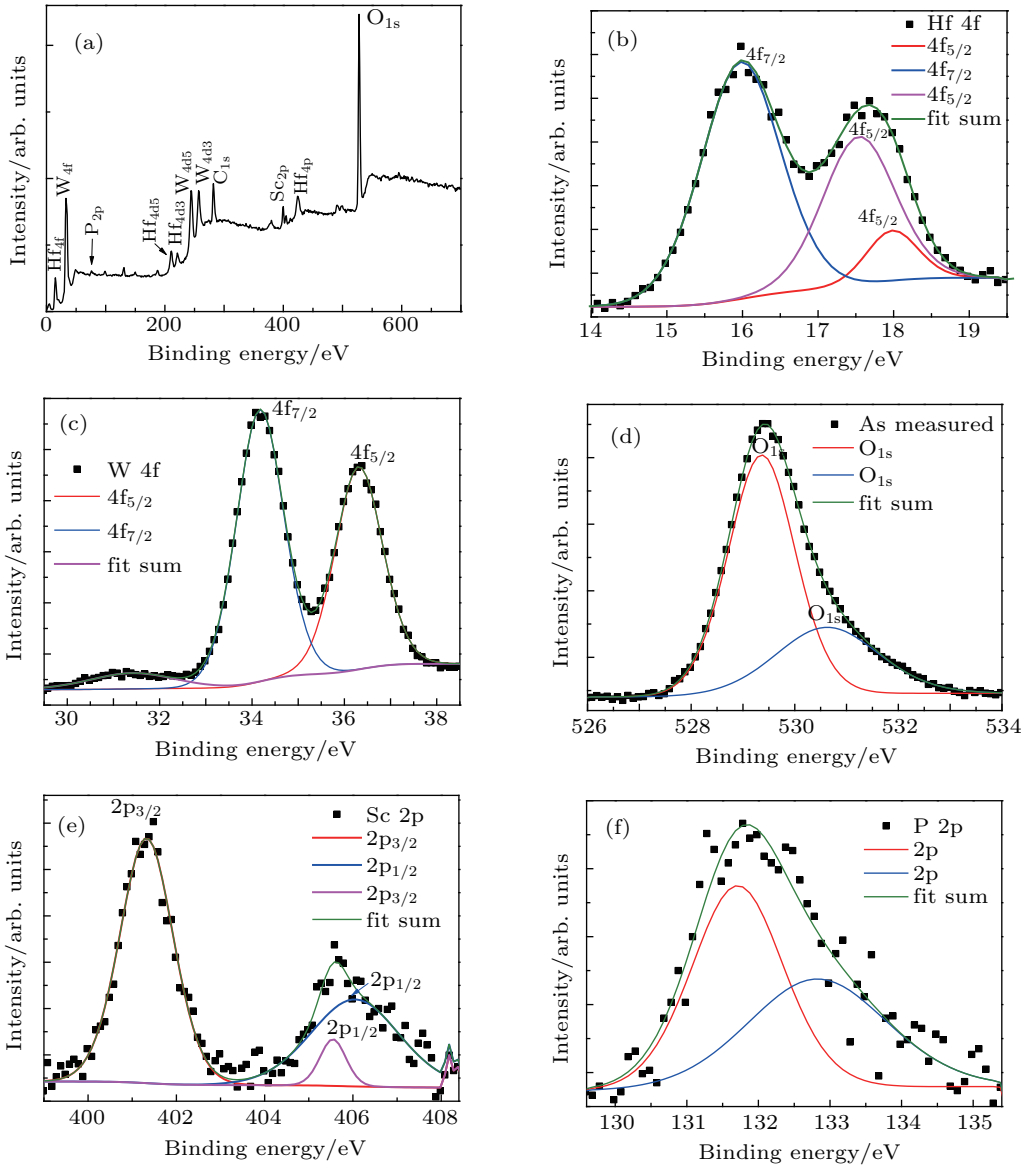


Fig. 2. (color online) (a) Survey scan XPS spectrum of the sample. (b)–(f) XPS spectra corresponding to the Hf 4f, W 4f, Sc 2p, O 1s, and P 2p orbitals.

Figure 2 shows the survey scan XPS spectrum and the XPS spectra corresponding to the Hf 4f, Sc 2p, W 4f, P 2p, and O 1s orbitals. Detailed analyses of the spectra (Figs. 2(b)–2(f)) show that the atomic ratio of Hf:Sc:W:P:O is about 4.73:4.31:14.27:5.32:71.38. Though the composition ratio is very close to the originally designed one for $HfScW_3PO_{15}$, considering its XRD pattern which suggests that the solid solution has a similar structure to $HfScW_2PO_{12}$,[37] it is preferred to write the formula of the solid solution as $(HfSc)_{0.83}W_{2.25}P_{0.83}O_{12-\delta}$. The excess W may occupy the position of (HfSc) in the unit cell.

3.2. Thermal expansion property

Figure 3 shows temperature-dependent XRD patterns of the solid solution from 94 K to 573 K. It is obvious that the diffraction peaks shift obviously toward larger 2θ values above 223 K, indicating a reduction in interplanar spacing. Lattice parameters at each temperature are calculated using the least-square method with the Powder X software. The changes of a, b, and c axes and cell volume with increasing temperature are illustrated in Figs. 4(a)–4(d), respectively. The results show that the b axis contracts continuously with increasing temperature in the whole temperature range measured while the a axis illustrates little change below 223 K and then contracts evidently above that temperature. Nevertheless, the c axis exhibits linear thermal expansion below 240 K and then deviates obviously from the linearity and finally becomes NTE with further increasing temperature. As a result, the cell volume behaves as a PTE below 255 K and an NTE above 255 K. The CTEs for the a, b, and c axes and volume in the NTE range are calculated to be -1.4×10^{-6} K^{-1}, -2.23×10^{-6} K^{-1}, -1.87×10^{-7} K^{-1}, and -3.10×10^{-6} K^{-1}, respectively. The linear CTE is $\alpha_l=\alpha_v/3=-1.03\times10^{-6}$ K^{-1}, confirming that $(HfSc)_{0.83}W_{2.25}P_{0.83}O_{12-\delta}$ is intrinsically a low NTE mate-

rial.

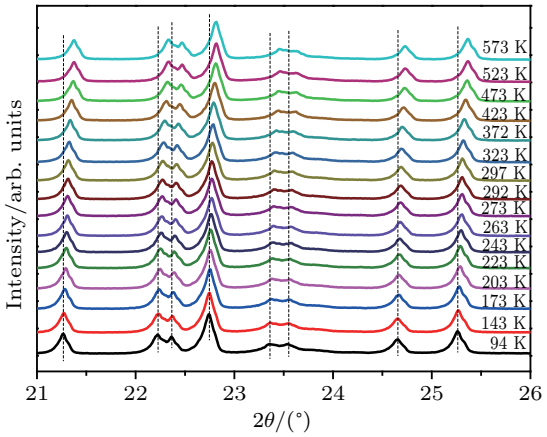


Fig. 3. (color online) Temperature-dependent XRD patterns from 94 K to 573 K. The measurement of 2θ is in a range of 10°–80° and only small range is shown for clarity.

Figures 5(a) and 5(b) show the relative length changes of a pellet of the solid solution with temperature increasing from 135 K to 673 K and from 293 K to 873 K and then cooled from 873 K to 322 K, respectively. It is obvious that its length increases as temperature rises from 135 K to about 273 K and then shrinks with further increase temperature, confirming the NTE property of this material. There is little thermal hysteresis between the heating and cooling process. From the relative length changes with temperature, the linear CTEs are calculated to be -1.21×10^{-6} K^{-1} (277 K–673 K), and -1.84×10^{-6} K^{-1} (294 K–790 K), respectively, which are in accordance with the XRD measurements. The difference of the CTEs measured by dilatometer from XRD could be due to the effect of the microstructures such as pores and cracks that are inevitable in the bulk material used for the dilatometric measurement. Figure 5(c) shows the SEM image of as-sintered sample. It consists of micron-sized particles with irregular sizes and shapes. The particles are closely packed but at the interfaces there appear a large number of pores formed probably during fast quenching.

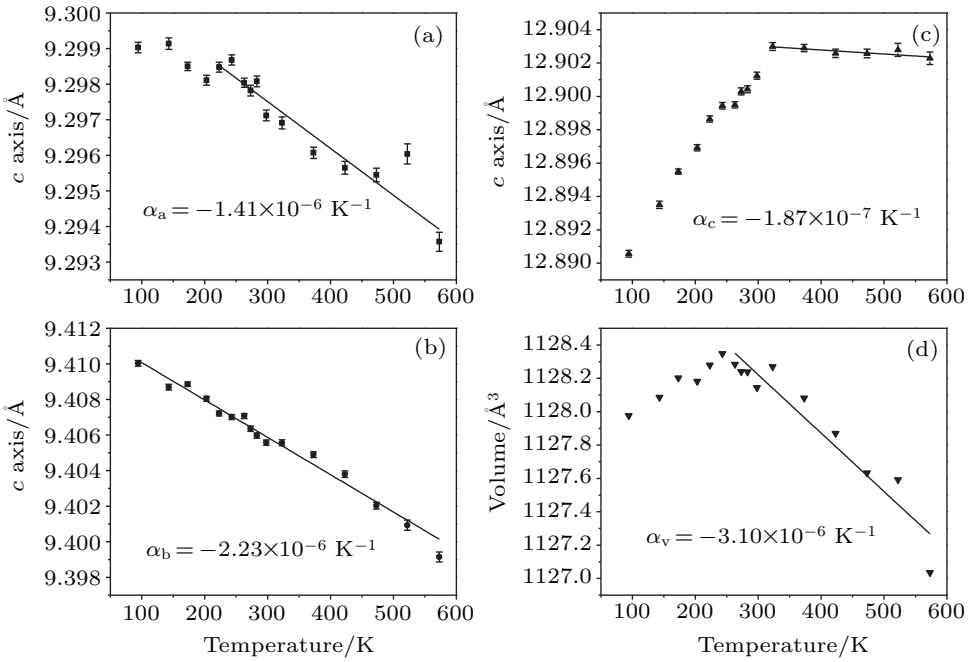


Fig. 4. Variations of lattice constants of the a, b, and c axes [panels (a)–(c) and cell volume (d) of $(HfSc)_{0.83}W_{2.25}P_{0.83}O_{12-\delta}$ with temperature.

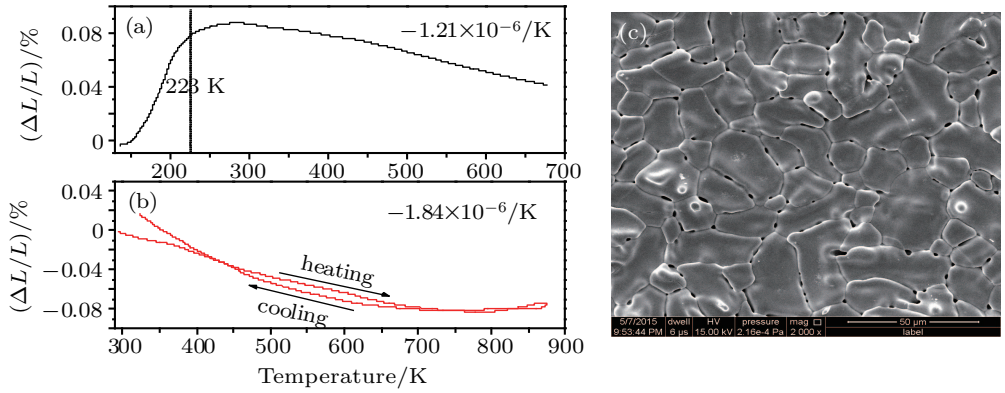


Fig. 5. (color online) Relative length changes of the synthesized cylinder with increasing temperature (a) from 135 K to 673 K and (b) from 293 K to 873 K and then cooled from 873 K to 322 K; (c) SEM image of the sintered sample.

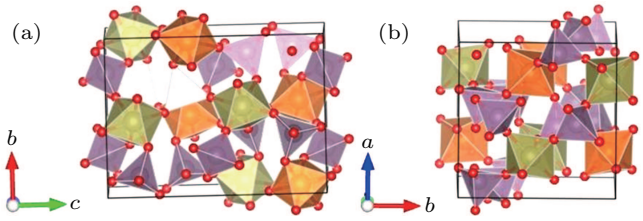


Fig. 6. (color online) Schematics of $(HfSc)_{0.83}W_{2.25}P_{0.83}O_{12-\delta}$ structure viewed from (a) the *a* and (b) the *c* axes directions.

In the orthorhombic structure, each HfO_6/ScO_6 octahedron shares its corners with WO_4/PO_4 tetrahedra or *vice visa*. According to previous studies on the orthorhombic structure of $HfMgW_3O_{12}$, and $HfMgW_{1.5}Mo_{1.5}O_{12}$, energetically the most stable configuration is that Hf and Mg are alternately aligned along the long axis[39] while W and Mo are mostly alternately arranged around each octahedron.[42] The material presented here can be regarded as the substitution of Mg by Sc and partial substitution of W by P in $HfMgW_3O_{12}$. Since its long axis is along the *c*-axis direction, we depict schematically the structure in Fig. 6. The corner-sharing nature of the polyhedra forms nonlinear Hf/Sc-O-W/P linkages. Transverse vibrations of the bridging O or the translational or librational vibrations of Hf/Sc and W/P bring the metal atoms at the two ends closer to each other. This is considered to be the origin of NTE in this material. It can be seen from Fig. 6(b) that most of the linkages are tilted along the *a*–*b* plane and hence transverse vibrations of the bridging O or the translational or librational vibrations of Hf/Sc and W/P lead to larger NTEs in the *a*- and *b*-axis directions and smaller NTE in the *c*-axis direction. Such vibrations correspond to low energy phonons generally below 300 cm^{-1}.

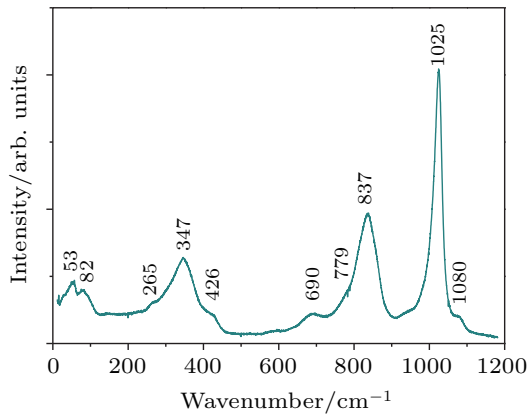


Fig. 7. (color online) Raman spectrum of $(HfSc)_{0.83}W_{2.25}P_{0.83}O_{12-\delta}$.

Figure 7 shows the Raman spectrum of the material, which confirms the existence of such vibrations as revealed by the Raman bands at 53, 62, and 256 cm^{-1}. The Raman modes at higher wave numbers resulting from asymmetric and symmetric bending (300 cm^{-1}–450 cm^{-1}), asymmetric and symmetric stretching (650 cm^{-1}–1100 cm^{-1}) modes in the WO_4/PO_4 tetrahedra have little contribution to the NTE.[17]

Thermal expansion anisotropy is defined as the largest difference in axial thermal expansion coefficients. The solid solution $(HfSc)_{0.83}W_{2.25}P_{0.83}O_{12-\delta}$ has a very low anisotropy in thermal expansion (2.04), even much lower than the lowest values of 5.12 ($Y_2Mo_3O_{12}$),[23] 6.5 ($ZrMgMo_3O_{12}$),[33] and 5.17 ($HfScW_2PO_{12}$)[37] for $A_2M_3O_{12}$, $AMgM_3O_{12}$, and $ABMXO_{12}$ family of materials, suggesting a high thermal shock resistance which is inversely proportional to the absolute value of CTE.[41] The very low anisotropy of thermal expansion in the present material is attributed to simultaneous contractions and low NTEs in all three axes.

3.3. Absorption and photoluminescence

Figure 8(a) shows the UV-vis absorption spectrum at RT. There is clearly a shoulder in the absorption spectrum which is recognized as an Urbach tail corresponding to localized excitons. Its optical band gap E_g^{op} can be determined from the absorption spectrum by using the Tauc formula $\alpha(h\nu) = A(h\nu + E_g^{op})^{1/2}$, where α is the absorption coefficient, $h\nu$ is the photon energy, and A is a constant. The optical band gap can be obtained by extrapolating the straight linear region to $\alpha^2(h\nu) = 0$. The band gap is estimated to be about 3.26 eV (corresponding to 381 nm in wavelength) from UV–vis absorption spectrum (see the insert in Fig. 8(a)).

Figures 8(b) and 8(c) present the photoluminescence spectra of $(HfSc)_{0.83}W_{2.25}P_{0.83}O_{12-\delta}$ from room temperature to 10 K with 340-nm light excitation. It is obvious that it possesses the intense broad band PL covering 370 nm–600 nm which can be deconvoluted into multiband. When the material is illuminated by photons with energy larger than the band gap, electrons would be excited from the valence band (VB) to the conduction band (CB) and then relaxed to the bottom of the CB, from where they transit back to the VB by direct recombination with the holes in the VB, or through the intermediate states. The PL band around 380 nm matches well with the band gap and hence can be attributed to the interband transitions from the bottom of CB to the top of VB. The rest of the PL bands with lower energies must be correlated to the energy states residing in the band gap. The Urbach tail in the UV–vis absorption spectrum suggests strongly that there exist intermediate states. The possible transitions are from CB to the acceptor states, from the donor states to the VB, and from donor–acceptor pairs as indicated in the insert of Fig. 8(c). In Fig. 8(d) we present the Commission Internationale de I'Eclairage (CIE) chromaticity coordinates of the PL at different temperatures. Its CIE chromatic coordinates vary gradually from (0.17, 0.12) at room temperature to (0.17, 0.19) at 10 K, which is larger than (0.159, 0.083) at room temperature and (0.17, 0.093) at 10 K of $HfScW_2PO_{12}$.

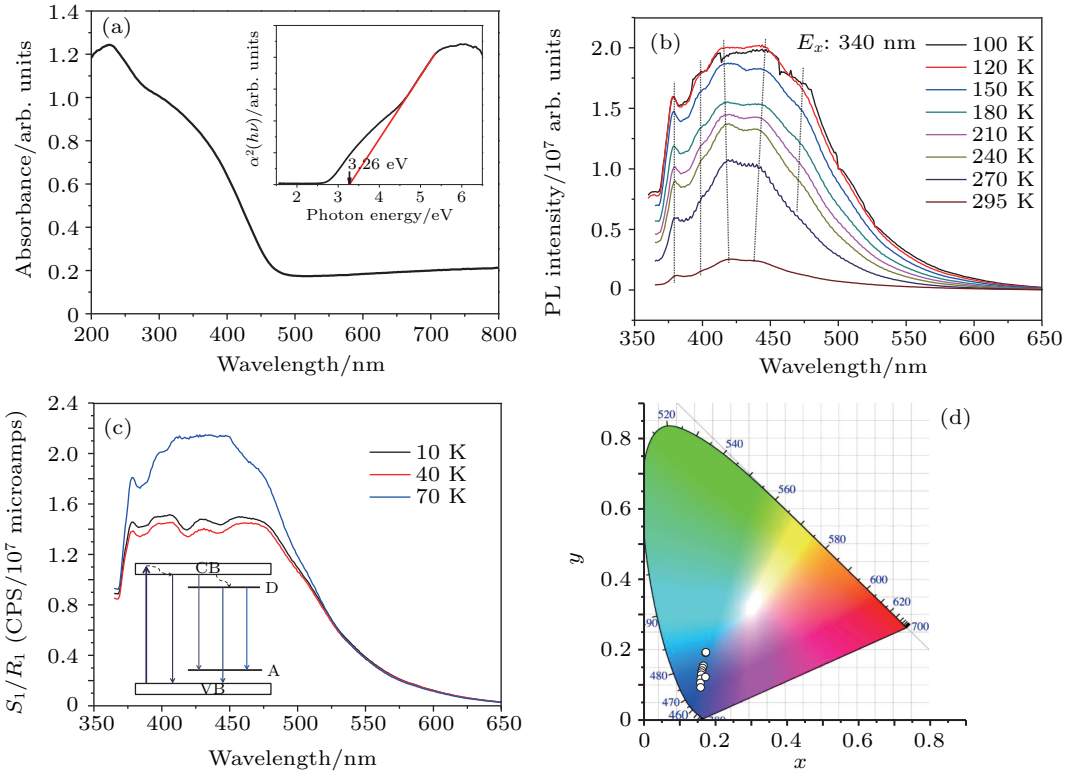


Fig. 8. (color online) Optical properties of $(HfSc)_{0.83}W_{2.25}P_{0.83}O_{12-\delta}$: (a) UV–vis absorption spectrum; ((b) and (c)) PL spectra at different temperatures; (d) Commission Internationale de I'Eclairage (CIE) chromaticity coordinates of the PL at different temperatures.

Figure 8(b) shows that the band gap remains unchanged with temperature decreasing but the other PL bands shift slightly toward shorter wavelengths and obviously toward longer wavelengths, respectively. The blue and red shifts must be correlated with shifts of the intermediate energy states, i.e. the donor and acceptor states when the temperature is changed. As mentioned above, the material presented here can be regarded as the substitution of Sc^{3+} for Mg^{2+} and partial substitution of $P^{5+}$for W^{6+} in $HfMgW_3O_{12}$. Such substitutions lead to a donor and acceptor co-doping effect. The Coulombic and van der Waals interactions between a donor and an acceptor depend on the donor–acceptor separation, which can be described as

$$E_{DA} = -\frac{e^2}{\varepsilon r_{DA}} - \left(\frac{e^2}{\varepsilon}\right)\left(\frac{a}{r_{DA}}\right)^6, \quad (1)$$

where r_{DA} is the distance between the donor and acceptor, ε is the dielectric constant, a is the effective van der Waals coefficient for the interaction between neutral donor and neutral acceptor. It should be mentioned that the donors and acceptors are localized in the centers of octahedra and tetrahedra, respectively, and hence the changes of their separations with temperature are dependent on axial CTE. Because of the difference in CTEs along different directions, the interaction energies develop with temperature at different rates, for the donor and acceptor pairs (DAPs) orient along different directions. The PL energy correlated with the DAP states is determined from[35,43]

$$h\nu = E_g - (E_D + E_A + E_{DA}), \quad (2)$$

where E_D and E_A are the donor and acceptor levels measured from the bottom of CB and from the top of VB, respectively. For the DAPs oriented along the b axis or a–b plane, obvious red shifts of the PL with temperature decreasing are expected due to the NTE nature of the b axis or a–b plane. Nevertheless, a blue shift is expected for the DAPs oriented along the c axis due to its PTE nature in the low temperature range.

4. Conclusions

A solid solution of $(HfSc)_{0.83}W_{2.25}P_{0.83}O_{12-\delta}$ is synthesized by high temperature solid state reaction and fast quenching method. It possesses an orthorhombic structure with space group *Pmmm* (47) at room temperature with lattice constants $a = 9.2439$ Å, $b = 9.4040$ Å, and $c = 12.9011$ Å. The CTEs for the a, b, and c axes and volume are calculated to be -1.41×10^{-6} K^{-1}, -2.23×10^{-6} K^{-1}, -1.87×10^{-6} K^{-1}, and -3.10×10^{-6} K^{-1}, respectively. This gives rise to a linear CTE of -1.03×10^{-6} K^{-1}. It displays also much lower thermal expansion anisotropy than the $A_2M_3O_{12}$ family of materials ever reported. Besides, it has intense photoluminescence from 360 nm to about 600 nm. The shifts of the PL peaks are closely correlated with axial thermal expansion property. The low CTEs with very low anisotropy in thermal expansion and

intense PL of the solid solution may find applications in optical devices such as white-light LEDs and in solid-state oxide fuel cells, etc.

References

[1] Mary T A, Evans J S O, Vogt T and Sleight A W 1996 *Science* **272** 90
[2] Tong P, Wang B S and Sun Y P 2013 *Chin. Phys. B* **22** 067501
[3] Chen J, Hu L, Deng J X and Xing X R 2015 *Chem. Soc. Rev.* **44** 3522
[4] Goodwin A L, Calleja M, Conterio M J, Dove M T, Evans J S O, Keen D A, Peters L and Tucker M G 2008 *Science* **319** 794
[5] Bridges F, Keiber T, Juhas P, Billinge S J L, Sutton L, Wilde J and Kowach G R 2014 *Phys. Rev. Lett.* **112** 045505
[6] Li C W, Tang X L, Mu?oz J A, Keith J B, Tracy S J, Abernathy D L and Fultz B 2011 *Phys. Rev. Lett.* **107** 195504
[7] Marinkovic B A, Ari M, Avillez R R, Rizzo F, Ferreira F F, Miller K J, Johnson M B and White M A 2009 *Chem. Mater.* **21** 2886
[8] Liu X, Cheng Y, Liang E and Chao M 2014 *Phys. Chem. Chem. Phys.* **16** 12848
[9] Ding P, Liang E J, Jia Y and Du Z Y 2008 *J. Phys.: Condens. Matter* **20** 275224
[10] Li W, Huang R J, Wang W, Liu H M, Han Y M, Huang C J and Li L F 2015 *J. Alloys Compd.* **628** 308
[11] Chu L H, Wang C, Yan J, Na Y Y, Ding L, Sun Y and Wen Y C 2012 *Scr. Mater.* **67** 173
[12] Tan J, Huang R J, Li W, Han Y M and Li L F 2014 *J. Alloys Compd.* **593** 103
[13] Tong P, Louca D, King G, Llobet A, Lin J C and Sun Y P 2013 *Appl. Phys. Lett.* **102** 041908
[14] Yamada I, Marukawa S, Murakami M and Mori S 2014 *Appl. Phys. Lett.* **105** 231906
[15] Azuma M, Chen W, Seki H, Czapski M, Olga S, Oka K, Mizumaki M, Watanuki T, Ishimatsu N, Kawamura N, Ishiwata S, Tucker M G, Shimakawa Y and Attfield J P 2011 *Nat. Commun.* **2** 347
[16] Chen J, Wang F F, Huang Q Z, Hu L, Song X P, Deng J X, Yu R B and Xing X R 2013 *Sci. Rep.* **3** 2458
[17] Liang E J, Liang Y, Zhao Y, Liu J and Jiang Y 2008 *J. Phys. Chem. A* **112** 12582
[18] Evans J S O, Hanson J C and Sleight A W 1998 *Acta Cryst. B* **54** 705
[19] Yuan B H, Liu X S, Mao Y C, Wang J Q, Guo J, Cheng Y G, Song W B, Liang E J and Chao M J 2016 *Mater. Chem. Phys.* **170** 162
[20] Yuan B H, Yuan H L, Song W B, Liu X S, Cheng Y G, Chao M J and Liang E J 2014 *Chin. Phys. Lett.* **31** 076501
[21] Liang Y, Xing H Z, Chao M J and Liang E J 2014 *Acta Phys. Sin.* **63** 248106 (in Chinese)
[22] Woodcock D A, Lightfoot P and Ritter C 2000 *J. Solid State Chem.* **149** 92
[23] Sumithra S and Umarji A M 2006 *Solid State Sci.* **8** 1453
[24] Liang E J, Huo H L, Wang J P and Chao M J 2008 *J. Phys. Chem. C* **112** 6577
[25] Hu L, Chen J, Sanson A, Wu H, Rodriguez C G, Olivi L, Ren Y, Fan L L, Deng J X and Xing X R 2016 *J. Am. Chem. Soc.* **138** 8320
[26] Miller K J, Romao C P, Bieringer M, Marinkovic B A, Prisco L and White M A 2013 *J. Am. Ceram. Soc.* **96** 561
[27] Cheng Y G, Mao Y C, Liu X S, Yuan B H, Chao M J and Liang E J 2016 *Chin. Phys. B* **25** 086501
[28] Suzuki T and Omote A 2004 *J. Am. Ceram. Soc.* **87** 1365
[29] Gindhart A M, Lind C and Green M 2008 *J. Mater. Res.* **23** 210
[30] Baiz T I, Gindhart A M, Kraemer S K and Lind C 2008 *J. Sol-Gel. Sci. Technol.* **47** 128
[31] Li F, Liu X S, Song W B, Yuan B H, Cheng Y G, Yuan H L, Cheng F X, Chao M J and Liang E J 2014 *J. Solid State Chem.* **218** 15
[32] Marinkovic B A, Jardim P M, Ari M, Avillez R R, Rizzo F and Ferreira F F 2008 *Phys. Stat. Sol.* **245** 2514
[33] Song W B, Liang E J, Liu X S, Li Z Y, Yuan B H and Wang J Q 2013 *Chin. Phys. Lett.* **30** 126502
[34] Ge X H, Mao Y C, Li L, Li L P, Yuan N, Cheng Y G, Guo J, Chao M J and Liang E J 2016 *Chin. Phys. Lett.* **33** 046503
[35] Ge X H, Mao Y C, Liu X S, Cheng Y G, Yuan B H, Chao M J and Liang E J 2016 *Sci. Rep.* **6** 24832
[36] Cheng Y G, Liang Y, Ge X H, Liu X S, Yuan B H, Guo J, Chao M J and Liang E J 2016 *RSC Adv.* **6** 53657
[37] Cheng Y G, Liang Y, Mao Y C, Ge X H, Yuan B H, Guo J, Chao M J and Liang E J 2017 *Mater. Res. Bull.* **85** 176
[38] Ge X H, Liu X S, Cheng Y G, Yuan B H, Chen D X, Chao M J, Guo J, Wang J Q and Liang E J 2016 *J. Appl. Phys.* **120** 205101
[39] Omote A, Yotsuhashi S, Zenitani Y and Yamada Y 2011 *J. Am. Ceram. Soc.* **94** 2285
[40] Dubois F, Goutenoire F, Laligant Y, Suard E and Lacorre P 2001 *J. Solid State Chem.* **159** 228
[41] Prisco L P, Ponton P I, Guaman M V, Avillez R R, Romao C P, Johnson M B, White M A and Marinkovic B A 2016 *J. Am. Ceram. Soc.* **99** 1742
[42] Li T, Ge X H, Liu X S, Cheng Y G, Liu Y M, Yuan H L, Li S L, Liu Y Y, Guo J, Li Y X and Liang E J 2016 *Mater. Express* **6** 515
[43] Hopfield J J, Thomas D G and Gershenzon M 1963 *Phys. Rev. Lett.* **10** 62